strength. The spectral dependence of calculated permeability is also described well by the 'Pendry-type' expression[7,10] $\mu(\lambda) = 1 + f_a\lambda_a^2/(\lambda^2 - \lambda_a^2 - i\lambda\Delta\lambda_a)$, where λ_a, $\Delta\lambda_a$ and f_a are the same notations as above but for the antisymmetric resonance (see Supplementary Information for details). The combination of these dispersion relations with the Fresnel's reflection coefficients for a thin anisotropic film placed on a glass substrate[25,26] leads to relatively simple expressions that can be used to fit the experimental spectra and find ε and μ. For example, in the case of Fig. 2c, the best fit to its spectra yields $\chi' \approx -0.5$ ($\mu' \approx 0.5$) near $\lambda = 470$ nm and corroborates the results of the Fernlab calculations (see Fig. 4). Similarly, the spectra for the samples covered with a glycerine film and showing an increased strength in the antisymmetric resonance yielded a significant increase in $|\chi|$, such that negative values of μ' were achieved almost routinely. For example, χ' was about -1.3 at the green resonance in Fig. 2a (that is, $\mu' \approx -0.3$). Although our structures exhibited both negative μ' and negative ε' within the same range of λ (for example, $\varepsilon' \approx -0.7$ and $\mu' \approx -0.3$ at the green resonance in Fig. 2a), μ had a rather large imaginary component ($\mu'' \equiv \mathrm{Im}(\mu) \approx 1i$ at the resonance), which so far has not allowed the observation of negative refraction.

We have however observed another effect—optical impedance matching—that is more tolerant to dissipation but also exclusive to materials with a finite permeability. The effect of impedance matching is characterized by the total suppression of reflection from an interface between two media with different refraction indices, $n = (\varepsilon\mu)^{1/2}$, but the same impedance values, $Z = (\varepsilon/\mu)^{1/2}$. This impedance matching is well known for electrical and microwave circuits but was never observed for conventional optics, because it requires $\mu \neq 1$ (except for singular cases of optical waveguides[27]), which has been unachievable until now. In our case, this phenomenon resulted in a total invisibility of our structured films at green-resonance frequencies for TM polarization of incident light, while the films could still be seen by using phase contrast imaging or TE polarization. For brevity, the experiments are described in Supplementary Information.

Received 19 May; accepted 19 September 2005.

1. Veselago, V. G. The electrodynamics of substances with simultaneously negative values of permittivity and permeability. *Sov. Phys. Usp.* **10**, 509–514 (1968).
2. Pendry, J. B. Negative refraction makes a perfect lens. *Phys. Rev. Lett.* **85**, 3966–3969 (2000).
3. Shelby, R. A., Smith, D. R. & Schultz, S. Experimental verification of a negative index of refraction. *Science* **292**, 77–79 (2001).
4. Smith, D. R., Padilla, W. J., Vier, D. C., Nemat-Nasser, S. C. & Schultz, S. Composite medium with simultaneously negative permeability and permittivity. *Phys. Rev. Lett.* **84**, 4184–4187 (2000).
5. Pendry, J. B. Positively negative. *Nature* **423**, 22–23 (2003).
6. Houck, A. A., Brock, J. B. & Chuang, I. L. Experimental observations of a left-handed material that obeys Snell's law. *Phys. Rev. Lett.* **90**, 137401 (2003).
7. Pendry, J. B., Holden, A. J., Robbins, D. J. & Stewart, W. J. Magnetism from conductors and enhanced nonlinear phenomena. *IEEE Trans. Microwave Theory Tech.* **47**, 2075–2084 (1999).
8. Wiltshire, M. C. K. *et al.* Microstructured magnetic materials for RF flux guides in magnetic resonance imaging. *Science* **291**, 849–851 (2001).
9. Pendry, J. B. & O'Brien, S. Magnetic activity at infrared frequencies in structured photonic crystals. *J. Phys. Condens. Matter* **14**, 6383–6394 (2002).
10. Yen, T. J. *et al.* Terahertz magnetic response from artificial materials. *Science* **303**, 1494–1496 (2004).
11. Linden, S. *et al.* Magnetic response of metamaterials at 100 terahertz. *Science* **306**, 1351–1353 (2004).
12. Landau, L. D. & Lifshitz, E. M. *Electrodynamics of Continuous Media* Section 60 (Oxford, Pergamon, 1960).
13. Dimmock, J. O. Losses in left-handed materials. *Opt. Express* **11**, 2397–2402 (2003).
14. Panina, L. V., Grigorenko, A. N. & Makhnovskiy, D. P. Metal-dielectric medium with conducting nanoelements. *Phys. Rev. B* **66**, 155411 (2002).
15. Podolskiy, V. A., Sarychev, A. K. & Shalaev, V. M. Plasmon modes in metal nanowires and left-handed materials. *J. Nonlinear Opt. Phys. Mater.* **11**, 65–74 (2002).
16. Prokhorov, A. M. Molecular amplifier and generator for submillimeter waves. *Zh. Eksp. Teor. Fiz.* **34**, 1658–1659 (1958).
17. Schawlow, A. L. & Townes, C. H. Infrared and optical masers. *Phys. Rev.* **112**, 1940–1949 (1958).
18. Aizpurua, J. *et al.* Optical properties of gold nanorings. *Phys. Rev. Lett.* **90**, 057401 (2003).
19. Jin, R. *et al.* Controlling anisotropic nanoparticle growth through plasmon excitation. *Nature* **425**, 487–490 (2003).
20. Barron, L. D. *Molecular Light Scattering and Optical Activity* (Cambridge Univ. Press, Cambridge, UK, 1982).
21. Kottmann, J. P. & Martin, O. J. F. Plasmon resonant coupling in metallic nanowires. *Opt. Express* **8**, 655–663 (2001).
22. Ebbesen, T. W., Lezec, H. J., Ghaemi, H. F., Thio, T. & Wolff, P. A. Plasmon-assisted transmission of entangled photons. *Nature* **391**, 667–669 (1998).
23. Feldj, N. *et al.* Enhanced substrate-induced coupling in two-dimensional gold nanoparticle arrays. *Phys. Rev. B* **66**, 245407 (2002).
24. Mock, J. J., Smith, D. R. & Schultz, S. Local refractive index dependence of plasmon resonance spectra from individual nanoparticles. *Nano Lett.* **3**, 485–491 (2003).
25. Born, M. & Wolf, E. *Principles of Optics* Section 2.3 (Cambridge Univ. Press, Cambridge, UK, 1980).
26. Abeles, F. in *Physics of Thin Films* Vol. 6 (eds Francombe, M. H. & Hoffman, R. W.) Ch. V–VII (Academic, New York, 1971).
27. Gademann, A., Durkan, C. & Shvets, I. V. Optical impedance matching with near-field optical microscopy. *J. Phys. D* **36**, 2193–2197 (2003).

Supplementary Information is linked to the online version of the paper at www.nature.com/nature.

Acknowledgements This research was supported by EPSRC (UK). We thank L. Panina and D. Makhnovskiy for discussions, and N. Roberts for collaboration in experiments. A.A.F. acknowledges support from INTAS.

Author Information Reprints and permissions information is available at npg.nature.com/reprintsandpermissions. The authors declare no competing financial interests. Correspondence and requests for materials should be addressed to A.N.G. (sasha@iman.ac.uk).

LETTERS

Spin-torque diode effect in magnetic tunnel junctions

A. A. Tulapurkar[1,2]†, Y. Suzuki[1,2,3], A. Fukushima[1,2], H. Kubota[1,2], H. Maehara[4], K. Tsunekawa[4], D. D. Djayaprawira[4], N. Watanabe[4] & S. Yuasa[1,2]

There is currently much interest in the development of 'spintronic' devices, in which harnessing the spins of electrons (rather than just their charges) is anticipated to provide new functionalities that go beyond those possible with conventional electronic devices. One widely studied example of an effect that has its roots in the electron's spin degree of freedom is the torque exerted by a spin-polarized electric current on the spin moment of a nanometre-scale magnet. This torque causes the magnetic moment to rotate[1–14] at potentially useful frequencies. Here we report a very different phenomenon that is also based on the interplay between spin dynamics and spin-dependent transport, and which arises from unusual diode behaviour. We show that the application of a small radio-frequency alternating current to a nanometre-scale magnetic tunnel junction[15–22] can generate a measurable direct-current (d.c.) voltage across the device when the frequency is resonant with the spin oscillations that arise from the spin-torque effect: at resonance (which can be tuned by an external magnetic field), the structure exhibits different resistance states depending on the direction of the current. This behaviour is markedly different from that of a conventional semiconductor diode[23], and could form the basis of a nanometre-scale radio-frequency detector in telecommunication circuits.

We performed experiments on a magnetic tunnel junction (MTJ) in the structure Si (substrate)/PtMn (15 nm)/CoFe (2.5 nm)/Ru (0.85 nm)/CoFeB (3 nm)/MgO (0.85 nm)/CoFeB (3 nm); see Fig. 1a. This multi-layered film was further patterned into oval-shaped pillars of dimension 200 nm × 100 nm, using electron-beam lithography and ion milling techniques. The bottom anti-ferromagnetically coupled CoFe and CoFeB layers (the synthetic antiferromagnetic layer) act as a pinned layer, while the top CoFeB layer acts as a free layer, whose magnetization can be changed. The resistance of the MTJ depends on the relative orientations of the pinned and free layers. The present MTJ shows a giant tunnelling magnetoresistance (TMR) due to the crystalline MgO (001) tunnelling barrier. A current passing through the MTJ gets spin-polarized by the pinned layer, and exerts a torque on the free layer.

The experimental arrangement to measure the diode effect is shown in Fig. 1a. A bias T is used to pass high-frequency current (200 MHz to 15 GHz) through the MTJ and to measure the d.c. voltage simultaneously. For all the experiments described here, the external magnetic field was applied at an angle of 30° from the pinned-layer magnetization axis within the film plane (see inset of Fig. 1b). In this geometry the sample showed a giant TMR of ~100%, as shown in Fig. 1b. We also measured microwave power from the MTJ arising from the thermal fluctuations of the free-layer magnetization[14,15]. The power was measured by a spectrum analyser, by passing a d.c. current of 1 mA using a bias T.

The radio frequency (r.f.) response of the MTJ was first tested using a network analyser. The results obtained showed evidence of magnetic resonance excited by r.f. current (results not shown).

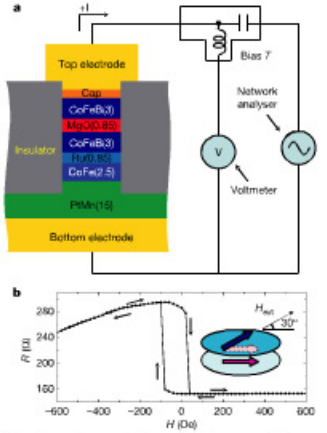

Figure 1 | Experimental set-up and magnetoresistance. a, Schematic diagram of the experimental set-up and cross-sectional view of the magnetic tunnel junction (MTJ) device. The thicknesses of various layers of the device in nanometres are given in brackets. The bottom CoFeB and CoFe layers, coupled anti-ferromagnetically through the Ru layer, act as a pinned layer. The top CoFeB layer acts as a free layer, the magnetization of which can be changed. The pinned and free layers are separated by a tunnelling MgO barrier. The experimental set-up measures the d.c. voltage produced across the device on applying the r.f. current. **b**, The magnetoresistance of the device, by applying magnetic field at 30° from the pinned-layer magnetization. The arrows indicate the sweeping direction of the magnetic field.

†Nanoelectronics Research Institute, National Institute of Advanced Industrial Science and Technology (AIST), Tsukuba 305-8568, Japan. ‡CREST, Japan Science and Technology Agency (JST), 4-1-8 Honcho, Kawaguchi 332-0012, Japan. §Graduate School of Engineering Science, Osaka University, 1-3 Machikaneyama, Toyonaka, Osaka 560-8531, Japan. ‖Electron Device Equipment Division, Canon ANELVA Corporation, 5-8-1 Yotsuya, Fuchu, Tokyo 183-8508, Japan. ¶Present address: Stanford Linear Accelerator Center, Stanford University, California 94025, USA.

Current-induced resonance has recently been observed also in a magnetic domain wall in the megahertz frequency range[20]. The signal is, however, small, and its phase determination is prone to errors in the calibration of the network analyser. In contrast, we found that the MTJ produces d.c. voltage because of its nonlinear behaviour and this diode-effect measurement offers phase-problem-free results. The effect of alternating current (a.c.) on the precession of magnetization induced by large d.c. current has recently[19] been studied. However, in the present experiment, we excite the magnetization only with alternating current, without applying a d.c. bias. The d.c. voltage response measured by passing 0.55 mA of r.f. current is plotted in Fig. 2. The response shows a large resonance structure, whose position depends on the magnetic field. Figure 3a shows the noise power spectra having a large peak, along with a small side peak, the positions of which also depend on the magnetic field.

The working principles of the spin-torque diode and the semiconductor p–n junction diode are compared in Fig. 4a. As shown in Fig. 4a, when current flows from the n side to the p side, the space charge region around the p–n junction is enlarged, and so the resistance of the p–n junction is higher in this case. For the opposite direction of current, the space charge region is shrunk, which gives lower resistance. In the case of the spin-torque diode, the alternating current passing through it exerts a torque on the free-layer spin moment. When the frequency of the alternating current nears the precession frequency of the free-layer spin-moment, the spin is tilted towards the pinned-layer magnetization during the negative (or positive) half of the alternating current. This configuration has low resistance. During the next half of the alternating current, spin is tilted in the opposite direction, which is a high-resistance state. The difference in resistance during positive and negative currents produces d.c. voltage, in the case of both the diodes. In contrast to the semiconductor diode, the spin-torque diode is resistant to the noise because it produces d.c. voltage only in a narrow frequency range around the resonance frequency, which can be tuned by applying a magnetic field.

Furthermore, the spin-torque diode effect is phase-sensitive. A small r.f. current ($I = I_{a.c.} \sin(2\pi ft)$) passing through MTJ exerts a torque on the free-layer spin. As a result, the z component (parallel to the pinned-layer magnetization) of the spin oscillates as $S_z = \cos(\theta) + A\sin(2\pi ft) + B\cos(2\pi ft)$, where A and B are respectively the in-phase and 90°-phase components of the motion of the spin, S_z denotes the direction cosine of the spin and θ is the angle between the free and pinned layers. The resistance of the MTJ depends on S_z as follows: $R = R_0 + 0.5^*\Delta R^*(1 - S_z)$, where R_0 is the resistance of the sample when the free layer is parallel to the pinned layer, and ΔR is the increase in the resistance when the free layer is anti-parallel to the pinned layer. The d.c. voltage given by the time-averaged value of I^*R is $V_{d.c.} = -A^*\Delta R^*I_{a.c.}/4$. Thus alternating current passing through the MTJ produces d.c. voltage, which is sensitive to the in-phase part of the oscillation of the magnetic moment. Because this is an intra-sample detection, it gives a phase-error-free spectrum, and a new method for performing ferromagnetic resonance experiments, for which at present an oscillating magnetic field is usually applied.

A torque exerted on the free-layer spin can in general be decomposed into two directions orthogonal to it, that is, $\dot{s}_{free} \times (\dot{s}_{free} \times \dot{s}_{pin})$ and $(\dot{s}_{free} \times \dot{s}_{pin})$, where $\dot{s}_{free}$ and $\dot{s}_{pin}$ are unit vectors along the magnetizations of the free and pinned layers respectively. The torque from the spin-transfer effect[1,2] lies in the first direction. The torque along the second direction is called the field-like term, and has been predicted in different ways[3,4]. Owing to the symmetry differences between these terms (when the free- and pinned-layer magnetizations are in-plane), the d.c. voltage produced by the spin-transfer torque shows a peak, whereas the d.c. voltage produced by an effective field shows a dispersion curve, as shown in Fig. 4b. If both torques act on the spin, by superposition, we get d.c. voltage, as shown in the bottom panel of Fig. 4b. For small and uniform oscillation of the magnetic moment, the d.c. voltage is given approximately by (see Supplementary Discussion):

$$V_{d.c.} \approx -\frac{1}{4}\Delta R \sin^2(\theta) I_{a.c.}^2 \,\mathrm{Re}\left[\frac{if\gamma' \mathrm{ST} - \gamma' H_k\, \gamma' \mathrm{FT}}{(f_0^2 - f^2) - if\alpha\gamma' H_d}\right] \qquad (1)$$

where ST is the spin transfer and FT is the effective field term, per unit current. γ is the gyromagnetic ratio ($\gamma' \equiv -\gamma/2\pi > 0$), α is the Gilbert damping factor, H_d is the demagnetization field perpendicular to the free-layer plane, f_0 is the resonant frequency and f is the frequency of the applied alternating current, $I_{a.c.}$. (We have neglected the stray field effect for a uniform mode.)

The comparison of the d.c. voltage and thermal noise power spectrum at 300 Oe is shown in Fig. 3b. Each spectrum is composed of a large resonance centred at about 7.5 GHz and a small resonance at lower frequency. Here we consider only the dominant resonance (larger peak in the noise) as the uniform oscillation of the free layer (see Supplementary Fig. 1). The d.c. voltage from this mode corresponds to a combination of spin-transfer and effective-field torques (compare with the bottom trace in Fig. 4b). The resonance frequency obtained from fitting to a superposition-type spectrum coincides with the main peak position in the thermal noise spectrum. The frequency of the resonance position as a function of magnetic field is plotted in Fig. 3c. For small θ, and neglecting the marginal influence of d.c. bias current, the resonance frequency is approximately given by Kittel's equation[17]: $f = \gamma'[(H_c + |H_{dip} + H_{ext}|)(H_c + H_d + |H_{dip} + H_{ext}|)]^{1/2}$, where H_c is the coercivity and H_{dip} is the dipolar field from the pinned layer. The fitting to this equation gives $H_c + H_{dip} = 176$ Oe and $H_d = 12.8$ kOe.

As mentioned above, because d.c.-measurement is phase-sensitive detection, we can decompose the spectra into two sources of torque—spin transfer and effective field—by using equation (1); see Supplementary Fig. 2. Further, we also measured the d.c. response by changing the r.f. current (see Fig. 3d), and found that the d.c. voltage decreased linearly with the square of the current, as expected from equation (1).

The d.c. voltage output of an ideal semiconductor diode is given by $V_{d.c.} \approx eV_{r.f.}^2/k_B T$, where $V_{r.f.}$ is the high-frequency voltage applied to the diode, k_B is Boltzmann's constant and T is the temperature. The

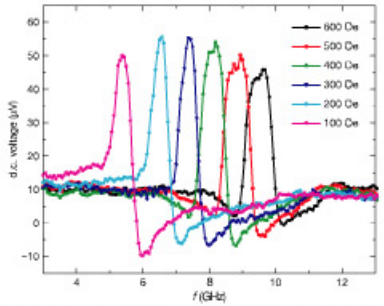

Figure 2 | Direct-current voltage generated by the device in response to the alternating current. The d.c. voltage is plotted as a function of the frequency of the a.c. current (0.55 mA). The external magnetic fields are as shown. The d.c. voltage results from the resonant oscillation of the magnetic moment of the free layer by current-induced spin-transfer and effective-field torques.

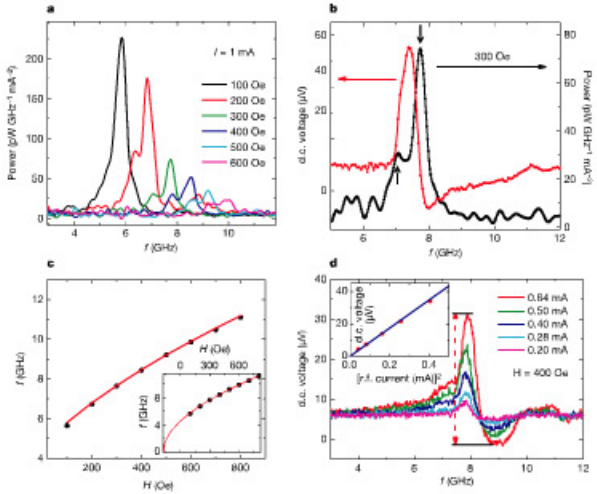

Figure 3 | Magnetic-field dependence of microwave power and a.c. current dependence of d.c. voltage. **a**, Microwave power spectra of the device measured by spectrum analyser, using a d.c. bias current of 1 mA. The power spectra with zero d.c. current are taken as background and subtracted from the data. The external magnetic fields are as shown. **b**, Comparison of the d.c. voltage spectrum and microwave power spectrum at 300 Oe. The arrows mark the positions of two peaks in the microwave power. The d.c. spectrum also has two corresponding resonance frequencies. The shape of the d.c. spectrum is a combination of peak and dispersion curves (also see Fig. 4b). Thus, the resonance positions do not match with the maxima in the d.c. voltage. **c**, The magnetic-field dependence of resonant frequency corresponding to the larger peak in the microwave power spectra. The black points represent the experimental data points, while the red curve is the fit to the data using Kittel's equation. The inset shows the extrapolation of the fitted curve to zero frequency. **d**, Direct-current voltage from a different sample for the given a.c. currents. The inset shows the linear power dependence of the d.c. voltage measured from peak to valley, as marked by the arrow in the main panel.

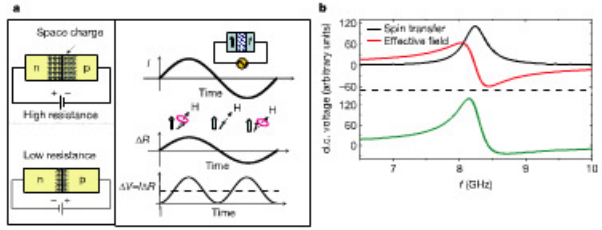

Figure 4 | Principle of the spin-torque diode. **a**, Comparison of the functioning of the semiconductor p–n diode (left panel) and the spin-torque diode (right panel). In the semi-conductor diode, if positive voltage is applied to the n side, the space charge region around the p–n junction is enlarged, and the resistance is high. For the opposite polarity, the space charge region is shrunk and the resistance is low. In the case of the spin-torque diode, the free-layer magnetization (shown by thin black arrows) oscillates owing to the current-induced torque. The resistance of the diode is less when the a.c. current is negative, because the free layer makes a smaller angle with the pinned layer (shown by the thick blue arrow). When the alternating current is positive, the resistance is larger, owing to the larger angle. The bottom trace in the right panel of **a** shows the schematic variation of the product of the current and the change in resistance. The dotted line shows the average value of this product, which appears as d.c. voltage across the spin-torque diode. **b**, Theoretical plot of the d.c. voltage spectrum obtained from equation (1). The d.c. voltage shows a peak if the torque induced by the a.c. current is due to the spin-transfer effect only. This is shown by the black curve in the top panel. But if the torque is due to the effective-field effect only, the d.c. voltage shows a dispersion curve, as shown by the red curve. If both the torques apply, the d.c. voltage shows a superposition of peak and dispersion, as shown by the green curve in the bottom panel.

spin-torque diode can perform r.f. detection better than the semiconductor diode if the magnetization of the pinned layer lies 45° out-of-plane. In this geometry, by increasing the ratio (H_0/H_c) of free-layer magnetization, we can squeeze the elliptical trajectory of the precession of the magnetic moment to lie in-plane. This enhances the amplitude of in-plane oscillation, and produces large d.c. voltage. The maximum d.c. voltage produced by spin-transfer in this case is given by (see Supplementary Discussion):

$$V_{d.c.} \approx \mathrm{TMR}\frac{V_{r.f.}^2}{V_c}\sqrt{\frac{H_4}{H_c}}$$

where V_c is the critical voltage required to flip the magnetization[3]. Thus, by increasing the H_4/H_c ratio as well as by increasing the magnetoresistance (as we have done here using a high-quality crystalline MgO barrier), the spin-torque diode can be a sensitive power detector. The sensitivity can also be enhanced by increasing the spin-transfer efficiency[16–19], which decreases the critical voltage.

Received 28 March; accepted 1 September 2005.

1. Slonczewski, J. C. Current-driven excitation of magnetic multilayers. *J. Magn. Magn. Mater.* **159**, L1–L7 (1996).
2. Berger, L. Emission of spin waves by a magnetic multilayer traversed by a current. *Phys. Rev. B* **54**, 9353–9358 (1996).
3. Zhang, S., Levy, P. M. & Fert, A. Mechanisms of spin-polarized current-driven magnetization switching. *Phys. Rev. Lett.* **88**, 236601 (2002).
4. Tatara, G. & Kohno, H. Theory of current-driven domain wall motion: spin transfer versus momentum transfer. *Phys. Rev. Lett.* **92**, 086601 (2004).
5. Kiselev, S. I. *et al.* Microwave oscillations of a nanomagnet driven by a spin-polarized current. *Nature* **425**, 380–383 (2003).
6. Rippard, W. H., Pufall, M. R., Kaka, S., Russek, S. E. & Silva, T. J. Direct-current induced dynamics in $Co_{90}Fe_{10}/Ni_{80}Fe_{20}$ point contacts. *Phys. Rev. Lett.* **92**, 027201 (2004).
7. Sun, J. Applied physics: spintronics gets a magnetic flute. *Nature* **425**, 359–361 (2003).
8. Myers, E. B., Ralph, D. C., Katine, J. A., Louie, R. N. & Buhrman, R. A. Current-induced switching of domains in magnetic multilayer devices. *Science* **285**, 867–870 (1999).
9. Tsoi, M. *et al.* Generation and detection of phase-coherent current-driven magnons in magnetic multilayers. *Nature* **406**, 46–48 (2000).
10. Tulapurkar, A. A. *et al.* Subnanosecond magnetization reversal in magnetic nanopillars by spin angular momentum transfer. *Appl. Phys. Lett.* **85**, 5358–5360 (2004).
11. Yagami, K., Tulapurkar, A. A., Fukushima, A. & Suzuki, Y. Low-current spin-transfer switching and its thermal durability in a low-saturation-magnetization nanomagnet. *Appl. Phys. Lett.* **85**, 5634–5636 (2004).
12. Koch, R. H., Katine, J. A. & Sun, J. Z. Time-resolved reversal of spin-transfer switching in a nanomagnet. *Phys. Rev. Lett.* **92**, 088302 (2004).
13. Urazhdin, S., Birge, N. O., Pratt, W. P. Jr & Bass, J. Current-driven magnetic excitations in permalloy-based multilayer nanopillars. *Phys. Rev. Lett.* **91**, 146803 (2003).
14. Özyilmaz, B. *et al.* Current-induced magnetization reversal in high magnetic fields in Co/Cu/Co nanopillars. *Phys. Rev. Lett.* **91**, 067203 (2003).
15. Grollier, J. *et al.* Spin-polarized current induced switching in Co/Cu/Co pillars. *Appl. Phys. Lett.* **78**, 3663–3665 (2001).
16. Katine, J. A., Albert, F. J., Buhrman, R. A., Myers, E. B. & Ralph, D. C. Current-driven magnetization reversal and spin-wave excitations in Co/Cu/Co pillars. *Phys. Rev. Lett.* **84**, 4212–4215 (2000).
17. Stiles, M. D. & Zangwill, A. Anatomy of spin-transfer torque. *Phys. Rev. B* **66**, 014407 (2002).
18. Lee, K.-J., Deac, A., Redon, O., Nozières, J.-P. & Dieny, B. Excitations of incoherent spin-waves due to spin-transfer torque. *Nature Mater.* **3**, 877–881 (2004).
19. Rufall, M. R., Rippard, W. H., Kaka, S., Silva, T. J. & Russek, S. E. Frequency modulation of spin-transfer oscillators. *Appl. Phys. Lett.* **86**, 082506 (2005).
20. Yuasa, S., Nagahama, T., Fukushima, A., Suzuki, Y. & Ando, K. Giant room-temperature magnetoresistance in single-crystal Fe/MgO/Fe magnetic tunnel junctions. *Nature Mater.* **3**, 868–871 (2004).
21. Parkin, S. S. P. *et al.* Giant tunnelling magnetoresistance at room temperature with MgO (100) tunnel barriers. *Nature Mater.* **3**, 862–867 (2004).
22. Djayaprawira, D. D. *et al.* 230% Room temperature magnetoresistance in CoFeB/MgO/CoFeB magnetic tunnel junctions. *Appl. Phys. Lett.* **86**, 092502 (2005).
23. Sze, S. M. *Physics of Semiconductor Devices* Ch. 2 (John Wiley & Sons, New York, 1981).
24. Smith, N. & Arnett, P. White-noise magnetization fluctuations in magnetoresistive heads. *Appl. Phys. Lett.* **78**, 1448–1450 (2001).
25. Nazarov, A. V., Cho, H. S., Nowak, J., Stokes, S. & Tabat, N. Tunable ferromagnetic resonance peak in tunneling magnetoresistive sensor structures. *Appl. Phys. Lett.* **81**, 4559–4561 (2002).
26. Saitoh, E., Miyajima, H., Yamaoka, T. & Tatara, G. Current-induced resonance and mass determination of a single magnetic domain wall. *Nature* **432**, 203–206 (2004).
27. Kittel, C. *Introduction to Solid State Physics* Ch. 16 (John Wiley & Sons, Singapore, 1996).
28. Jiang, Y. *et al.* Substantial reduction of critical current for magnetization switching in an exchange-biased spin valve. *Nature Mater.* **3**, 361–364 (2004).
29. Mangin, S., Ravelosona, D., Katine, J. A., Carey, M. J., Terris, B. D. & Fullerton, E. E. Current-induced magnetization reversal in nanopillars with perpendicular anisotropy. *Nature Mater.* **5**, 210–215 (2006).

Supplementary Information is linked to the online version of the paper at www.nature.com/nature.

Acknowledgements A.A.T. thanks the Japan Society for the Promotion of Science for the fellowship grant. S.Y. thanks the Japan Science and Technology Agency (JST) for the PRESTO programme. A part of this work is supported by the 21st Century COE programme by JSPS. We thank C. Chappert, T. Devolder, W. Mizutani and M. Mizuguchi for their help.

 Correspondence and requests for materials should be addressed to Y.S. (suzuki-y@mp.es.osaka-u.ac.jp).

LETTERS

Chaos-based communications at high bit rates using commercial fibre-optic links

Apostolos Argyris[1], Dimitris Syvridis[1], Laurent Larger[2], Valerio Annovazzi-Lodi[3], Pere Colet[4], Ingo Fischer[5]†, Jordi García-Ojalvo[6], Claudio R. Mirasso[7], Luis Pesquera[8] & K. Alan Shore[9]

Chaotic signals have been proposed as broadband information carriers with the potential of providing a high level of robustness and privacy in data transmission[1,2]. Laboratory demonstrations of chaos-based optical communications have already shown the potential of this technology[3–5], but a field experiment using commercial optical networks has not been undertaken so far. Here we demonstrate high-speed long-distance communication based on chaos synchronization over a commercial fibre-optic channel. An optical carrier wave generated by a chaotic laser is used to encode a message for transmission over 120 km of optical fibre in the metropolitan area network of Athens, Greece. The message is decoded using an appropriate second laser which, by synchronizing with the chaotic carrier, allows for the separation of the carrier and the message. Transmission rates in the gigabit per second range are achieved, with corresponding bit-error rates below 10^{-7}. The system uses matched pairs of semiconductor lasers as chaotic emitters and receivers, and off-the-shelf fibre-optic telecommunication components. Our results show that information can be transmitted at high bit rates using deterministic chaos in a manner that is robust to perturbations and channel disturbances unavoidable under real-world conditions.

Broadband information carriers enhance the robustness of communication channels to interferences with narrow-band disturbances. This is the basis of spread-spectrum communication techniques, such as the code division multiple access (CDMA) protocol used in the Global Positioning System (GPS) and in the third generation of mobile telephones. In chaos-based communications the broadband coding signal is generated at the physical layer instead of algorithmically. Additionally, chaotic carriers offer a certain degree of intrinsic privacy in the data transmission, which could complement (via robust hardware encryption) both classical (software-based)[6] and quantum[7] cryptography systems. From a fundamental viewpoint, using waveforms generated by deterministic chaotic systems to carry information in a robust manner that also allows high bit rates is a generalization of standard communication systems. It might also provide a deeper insight into the mechanism of transmission of information in natural systems with complex dynamics, such as biological systems.

Chaotic communication systems based on chaos synchronization[8] were proposed in the early 1990s (refs 1, 2). In this type of communication protocol, messages are embedded within a chaotic carrier in the emitter, and recovered after transmission by a receiver upon synchronization with the emitter. The receiver architecture can be viewed as performing a nonlinear filtering process, intended to

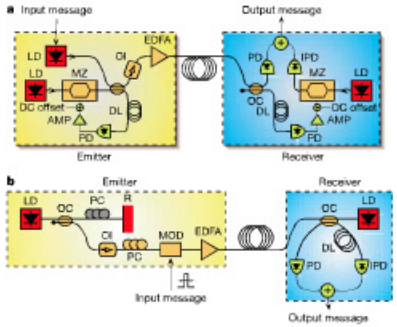

Figure 1 | Two schematic set-ups for optical chaos communication. In the optoelectronic scheme (**a**), the emitter is a laser diode (LD) whose output is modulated in a strongly nonlinear way by an electro-optic feedback loop through an integrated electro-optic Mach–Zehnder interferometer (MZ). The message is added inside the delay oscillation loop. An erbium-doped fibre amplifier (EDFA) is used to adjust the power to be injected into the transmission line. The EDFA is followed by an optical filter (not shown) that cuts off the amplified spontaneous emission noise. All LDs operate at around 1.55 μm. In the all-optical scheme (**b**), the emitter is a laser diode subject to optical feedback from a digital variable reflector (R). The length of the external cavity is 6 m; a polarization controller (PC) is used within the cavity to adjust the polarization state of the light reflected back from the variable reflector. The message is added via a modulator (MOD) at the emitter's output. A typical transmission module, represented by a fibre loop in the figure, consists of a combination of single-mode and dispersion-compensated fibres, followed by an EDFA that compensates for the power lost upon transmission. In both schemes, decoding is performed via subtraction of the transmitted signal from the signal filtered by the receiver. Operationally, the subtraction is performed by adding the photocurrents coming from an ordinary and a sign-inverting amplified photodiode (PD and IPD, respectively). Fibre connections are represented by thick lines, and electric connections by thin lines. Other elements in the diagram include optical isolators (OI), delay lines (DL), electronic amplifiers (AMP) and optical fibre couplers (OC).

[1]Department of Informatics, University of Athens, Athens 15784, Greece. [2]UMR CNRS 6174, FEMTO-ST / Optics, University of Franche-Comté, 16 route de Gray, 25030 Besançon cedex, France. [3]Department of Electronics, University of Pavia, 27100 Pavia, Italy. [4]Instituto Mediterráneo de Estudios Avanzados, (IMEDEA, CSIC-UIB), Campus UIB, E-07122 Palma de Mallorca, Spain. [5]Institute of Applied Physics, Darmstadt University of Technology, 64289 Darmstadt, Germany. [6]Departament de Física i Enginyeria Nuclear, Universitat Politècnica de Catalunya, E-08222 Terrassa, Spain. [7]Departament de Física, Universitat de les Illes Balears, E-07122 Palma de Mallorca, Spain. [8]Instituto de Física de Cantabria (CSIC-UC), Avd de los Castros s/n, E-39005 Santander, Spain. [9]School of Informatics, University of Wales, Bangor LL57 1UT, UK. †Present address: Department of Applied Physics and Photonics, Vrije Universiteit Brussel, Pleinlaan 2, 1050 Brussels, Belgium.